

Electron tomography reveals the fibril structure and lipid interactions in amyloid deposits

Marius Kollmer^{a,1}, Katrin Meinhardt^{a,1}, Christian Haupt^a, Falk Liberta^a, Melanie Wulff^a, Julia Linder^a, Lisa Handl^b, Liesa Heinrich^c, Cornelia Loos^a, Matthias Schmidt^a, Tatiana Syrovets^d, Thomas Simmet^d, Per Westermark^e, Gunilla T. Westermark^f, Uwe Horn^c, Volker Schmidt^b, Paul Walther^{g,2}, and Marcus Fändrich^{a,2}

^aInstitute of Protein Biochemistry, Ulm University, 89081 Ulm, Germany; ^bInstitute of Stochastics, Ulm University, 89081 Ulm, Germany; ^cLeibniz Institute for Natural Product Research and Infection Biology, Hans Knoell Institute, 07745 Jena, Germany; ^dInstitute of Pharmacology of Natural Products & Clinical Pharmacology, Ulm University, 89081 Ulm, Germany; ^eDepartment of Immunology, Genetics, and Pathology, Rudbeck Laboratory, Uppsala University, Uppsala SE-751 85, Sweden; ^fDepartment of Medical Cell Biology, Uppsala University, SE-75123 Uppsala, Sweden; and ^gCentral Electron Microscopy Facility, Ulm University, 89081 Ulm, Germany

Edited by Wolfgang Baumeister, Max Planck Institute of Biochemistry, Martinsried, Germany, and approved March 30, 2016 (received for review November 27, 2015)

Electron tomography is an increasingly powerful method to study the detailed architecture of macromolecular complexes or cellular structures. Applied to amyloid deposits formed in a cell culture model of systemic amyloid A amyloidosis, we could determine the structural morphology of the fibrils directly in the deposit. The deposited fibrils are arranged in different networks, and depending on the relative fibril orientation, we can distinguish between fibril meshworks, fibril bundles, and amyloid stars. These networks are frequently infiltrated by vesicular lipid inclusions that may originate from the death of the amyloid-forming cells. Our data support the role of nonfibril components for constructing fibril deposits and provide structural views of different types of lipid–fibril interactions.

aggregation | conformational disease | electron tomography | protein assembly | prion

Amyloid fibrils are fibrillary polypeptide aggregates with a cross- β conformation (1, 2) and define a group of debilitating human diseases that includes, besides Alzheimer's disease and type II diabetes, different forms of systemic amyloidosis (1, 3). Considerable previous research has focused on the structure of individual fibrils and determined their β -strand conformation (1, 4), their global topology, and the position of the polypeptide chains within the fibril (5), but comparatively little is known about how fibrils are organized into a 3D amyloid deposit.

Amyloid fibrils make, specifically in systemic amyloidosis, substantial contributions to the disease process and physically impair the functionality of the affected tissue (6, 7). The way in which fibrils are arranged can vary between different forms of a disease, suggesting that the deposit structure may contribute to the disease process. In systemic transthyretin (ATTR) amyloidosis, for example, the deposit structure was found to correlate with the Congo red (CR) staining properties and tissue involvement in different variants of the disease (8). In Alzheimer's disease, there is evidence that the amyloid β (A β) amyloid plaque structure in affected patients is histologically different from the A β plaques in the brains of nondemented individuals (9).

In this research, we have used electron tomography, an increasingly powerful method to characterize macromolecular assemblies and cellular structures at very high resolution (10), to investigate the network structure within an amyloid deposit. The analyzed amyloid deposits were formed by a cell culture model of systemic amyloid A (AA) amyloidosis (11–13), an amyloid disease that affects humans and other mammals, and birds (14). AA amyloid deposits occur in multiple organs and are frequently found in spleen, kidneys, and liver. AA amyloid fibrils consist of AA protein, a proteolytic fragment of serum amyloid A1 (SAA1) protein (14). This acute-phase protein is secreted by the liver in response to chronic inflammation and released into the blood, where it associates with high-density lipoprotein (HDL) particles. The cell model reproduces crucial features of fibril formation from

SAA1 protein in vivo, such as the involvement of macrophages (11); the fragmentation of SAA1 protein (15); and the association of fibrils with secondary components, such as glycosaminoglycans (GAGs) and lipids (13, 16). Due to its ready accessibility, we use it here for further analysis with electron tomography.

Our study shows that electron microscopy is a powerful technique that is able to visualize the fibril network structure and the fibril morphology directly in the deposits. The deposited filaments can adopt multiple network structures, and they are frequently infiltrated by vesicular lipid inclusions.

Results

Formation of Amyloid-Like Fibrils from SAA1 Protein in Cell Culture.

Exposure of murine J774A.1 cells, a widely used model of macrophage and monocytic function, to acute-phase levels of murine SAA1 protein and HDL was previously shown to lead to the formation of extracellular amyloid deposits (13). The formed amyloid deposits stain with CR (Fig. S1A) and produce green birefringence in the polarizing microscope (Fig. S1B), which is the gold standard of amyloid diagnosis in pathology (2). By using scanning electron microscopy (SEM), we here find that the formed amyloid deposits consist of extracellular fibrils that can be immunogold-labeled via a primary antibody raised against

Significance

Although considerable previous efforts have been dedicated to studying the molecular assembly of individual amyloid fibrils, much less is known about their 3D arrangement within a pathological deposit. In this study, we use electron tomography, an extremely powerful method for studying the detailed structure of cellular assemblies or macromolecular complexes, to unravel the superstructure of fibril networks. The structural views provided by our analysis enable a better understanding of the properties and pathogenic features of amyloid fibrils. The fibril network structure is also a crucial determinant of possible applications of such fibrils in the field of biotechnology or material sciences.

Author contributions: U.H., V.S., P. Walther, and M.F. designed research; M.K., K.M., F.L., M.W., J.L., L. Handl, M.S., and P. Walther performed research; C.H., F.L., L. Heinrich, C.L., T. Syrovets, T. Simmet, P. Westermark, G.T.W., U.H., and P. Walther contributed new reagents/analytic tools; M.K., K.M., F.L., M.W., L. Handl, M.S., V.S., P. Walther, and M.F. analyzed data; and M.K. and M.F. wrote the paper.

The authors declare no conflict of interest.

This article is a PNAS Direct Submission.

¹M.K. and K.M. contributed equally to this work.

²To whom correspondence may be addressed. Email: paul.walther@uni-ulm.de or marcus.fandrich@uni-ulm.de.

This article contains supporting information online at www.pnas.org/lookup/suppl/doi:10.1073/pnas.1523496113/-DCSupplemental.

full-length SAA1.1 protein (Fig. S1 C–E). Transmission electron microscopy (TEM) analysis of ultrathin sections further confirmed this finding and showed the immunogold labeling of the fibrils (Fig. S1F). The formed deposits comprise typical components of pathological AA amyloid deposits, and in addition to AA protein, they contain GAGs, which we demonstrate here with Alcian blue staining (Fig. S1G) and with antibody reacting with heparan sulfate (Fig. S1H), as well as a serum amyloid P (SAP) component (Fig. S1I).

Fibrils extracted from the deposits (Fig. S2A) consist of partially fragmented SAA1 protein (Fig. S2B), resembling the C-terminal truncation of SAA1 protein in AA amyloidosis (17). Similar C-terminal truncation was reported previously to occur if primary murine macrophages are exposed to SAA1 protein in vitro (15). The formed fibrils exhibit bona fide amyloid characteristics and give rise to X-ray reflections at $4.74 \pm 0.03 \text{ \AA}$ and $10.7 \pm 0.1 \text{ \AA}$ (Fig. S3A) that demonstrate the presence of a cross- β -sheet conformation. Extracted fibrils bind amyloid binding dyes, such as thioflavin T (Fig. S3B) and CR (Fig. S2C), and produce CR green birefringence in the polarizing microscope (Fig. S2C), similar to the properties of the amyloid deposits before fibril extraction (Fig. S1 A and B). This structure differs from globular SAA1 and SAA3 proteins (18, 19), which are significantly α -helical and devoid of β -sheet structure (Fig. S3C). These globular proteins exhibit an α -helical content of 70–74% as determined by the program DSSP, whereas attenuated total reflectance Fourier-transform infrared spectroscopy and deconvolution of the amide I spectral region reveal a β -sheet content of the presently analyzed fibrils of 73% (Fig. S3D). These data show that the protein has undergone a drastic conformational change as it converted into the fibril state.

Cell Culture Fibrils Are Toxic to Neighboring Cells. Addition of fibrils extracted from the cell culture to a fresh culture of J774A.1 cells induces cellular toxicity and metabolic changes, as demonstrated by the 2,5-diphenyltetrazolium bromide (MTT) assay (Fig. S4A), as well as apoptosis, as shown by increased caspase 3/7 activity (Fig. S4B). These effects were measured with cells kept without HDL-SAA1; that is, the cells do not themselves form amyloid, and the strength of the effect depends on the fibril concentration applied to the cells. Analysis of the mechanism underlying this effect with confocal laser-scanning microscopy shows that SAA1 fibrils from the cell culture that were fluorescently labeled with Alexa Fluor 488 dye are avidly taken up by the cells, where they accumulate at substantial levels (Fig. S4 C and D). Uptake occurs mainly via phagocytosis (Fig. S4E) and leads to the accumulation of fibrils in the endocytic pathway, where they cause lysosomal leakage and the disruption of intracellular membranes, as shown by a flow cytometric analysis of cells that had additionally internalized Acridine Orange (Fig. S4F). This dye shows a pH-dependent reduction of its fluorescence intensity as soon as it exits the lysosomes into the cytoplasm.

Electron Tomography Reveals the Deposit to Consist of Multiple Fibril Network Structures. We then prepared freeze-substituted specimens of the fibril deposits to cut out sections that we analyzed with scanning TEM at 300 kV. Based on image series with incrementally varied tilt angles, we computed the 3D tomograms of the analyzed amyloid deposits. The tomograms show well-resolved fibrils that could be tracked through multiple virtual sections (Fig. 1). The fibrils are arranged into networks that exhibit significant local order. We can discern three major types of networks that we term here the fibril meshwork, fibril bundle, and amyloid star. Fibril meshworks present no preferential overall orientation of the constituting filaments, whereas fibrils in a bundle are significantly aligned in parallel. An amyloid star consists of fibrils that radiate out in different x/y directions. However, analysis of different horizontal planes of the tomogram cannot reveal well-defined star

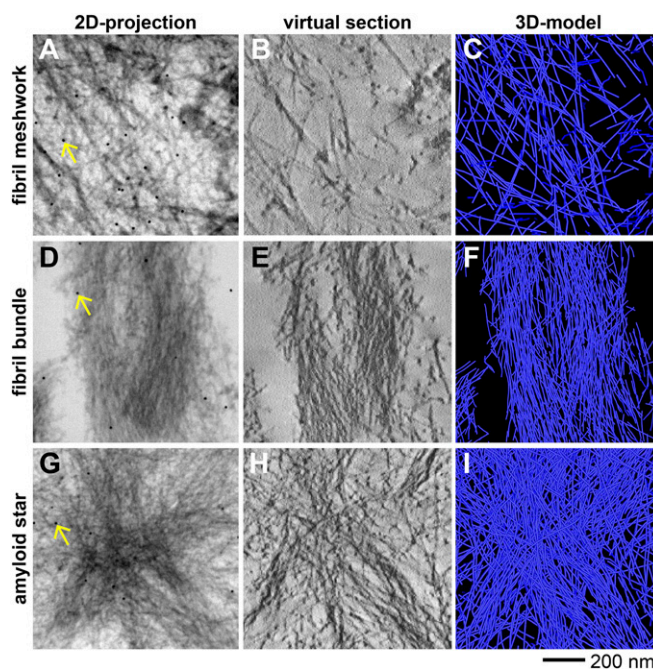


Fig. 1. Electron tomograms showing different fibril network structures. Fibril meshwork (*Top*), fibril bundle (*Middle*), and amyloid star (*Bottom*). (*Left*) Two-dimensional projections of a 500-nm-thick slice of a deposit. (*Center*) Virtual sections through the tomograms; thickness of the virtual sections: fibril meshwork = 1.29 nm, fibril bundle = 1.29 nm, and amyloid star = 1.84 nm. (*Right*) Three-dimensional model. Fibrils are shown in blue, and gold particles used for image alignment are shown as yellow arrows.

core and the star represents a stack of fibril bundles with different orientations relative to each other (Fig. S5). The three types of network structures usually co-occur within the same amyloid deposit (Fig. S6).

Morphological Analysis of the Fibrils Within the Deposit. We then measured, within our tomograms, the distribution of the fibril width W and the persistence length P , which reflect the bending propensity of the filament (Fig. 2A). The obtained values of W present a roughly bell-shaped distribution, centered at 11–12 nm (Fig. 2A). We obtained relatively similar distributions of W for the fibril meshwork, the fibril bundle, and the amyloid star (Fig. 2A). Also, the parameter P shows a very similar distribution for the fibrils in the three deposit structures (Fig. 2A), which, taken together with the similarity of W , suggests that the amyloid star, fibril bundle, and meshwork are constructed from morphologically similar fibrils.

The two properties W and P could also be measured with fibrils that were extracted from the cell culture; immobilized onto a formvar-carbon-coated grid; negatively stained; and viewed by conventional TEM techniques, that is, without using tomography (Fig. 2B). These measurements show a slightly higher average value of W than in the tomography-based measurements (Fig. 2A), presumably arising from the lateral association of counterstaining agent, whereas the distribution of the values of P corresponds well to the measurements performed on the fibrils in the deposit (Fig. 2A). By negative-stain TEM, we could also analyze that fibril morphology of filaments extracted from murine amyloidotic spleen (Fig. 2C) and the distribution of values for P and W resemble the distribution of values of cell culture fibrils (Fig. 2A). By contrast, we found much more pronounced differences when we compared cell culture fibrils with fibrils grown from pure SAA1 protein in simple phosphate buffer in vitro (Fig. 2D and Fig. S7B). These in vitro fibrils were formed according to a

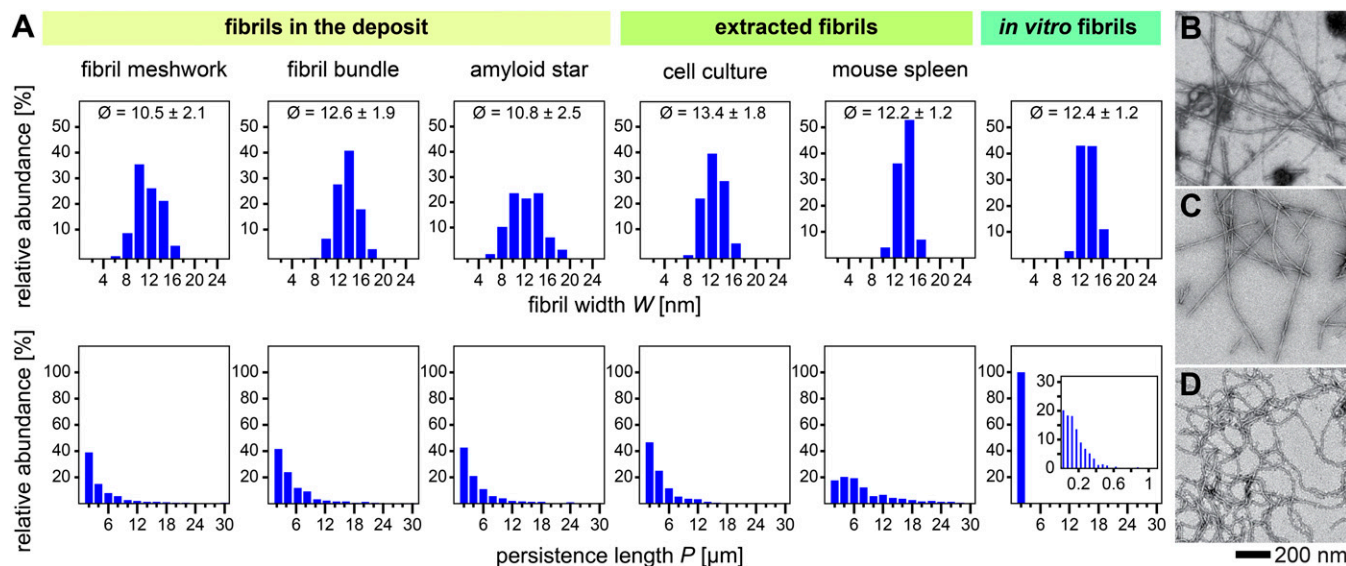


Fig. 2. Fibril morphology in the amyloid deposit. (A) Distribution of the values of fibril width (W) and persistence length (P) obtained from the tomograms of fibril deposits and by conventional TEM of fibrils extracted from the cell culture or murine AA amyloidotic spleen or of fibrils grown from pure SAA1 protein in vitro. (A, *insets*) Close-up view of the region of $P < 1 \mu\text{m}$. (B–D) TEM images of fibrils extracted from cell culture (B) and from mouse spleen (C) and of fibrils that were formed from pure SAA1 protein in vitro (D) are shown.

previously published protocol (20). They exhibit a relatively curvilinear structure in the original TEM images (Fig. 2D) and give rise to much smaller P values than cell culture-derived fibrils and AA amyloid fibrils (Fig. 2A).

We also tested other conditions of fibril formation in vitro, such as incubation of SAA1 protein at pH 7.4. However, the fibril yield obtained under this condition was much smaller than at pH 3.0, as judged from the amount of material visible on the TEM grid (Fig. S7). Seeding with 5% (vol/vol) murine ex vivo AA amyloid fibrils slightly increased the number of visible fibrils, but the amount of fibrous material attached to the grid remained low. The observed fibrils were relatively long and straight and resembled in their morphologies the AA fibrils that we used as seeds.

Amyloid Deposits Comprise Vesicular Lipid Inclusions. The formed deposits were frequently infiltrated by vesicular lipid inclusions that possess a hollow architecture and the typical double-layer structure of lipid membranes (Fig. S8A–D). The thickness of the bilayers ($7.3 \pm 0.7 \text{ nm}$; Fig. S8E) is also consistent with literature values for biological membranes (21–23). Lipids represent, besides SAP and GAGs, an additional class of nonfibril components of disease-associated, extracellular amyloid deposits (16, 24) and were previously shown to interact with many amyloid-forming polypeptide chains (25), to promote fibril formation in vitro (25), and to mediate the amyloid-dependent enhanced infectivity of HIV-1 to cultured cells (26).

Our tomograms now reveal that the lipid inclusions exhibit a vesicular organization with diameters ranging from 20 nm to sometimes over 500 nm. The overall guise of these inclusions encompassed elongated tubular networks to spherical structures and multivesicular assemblies. Some exhibited a particularly electron dense structure, resembling apoptotic bodies (Fig. 3A–D), which suggests that the inclusions originate from the death of the amyloid-producing cells. Indeed, caspase activity and MTT assay constitutively demonstrate fibril formation to be toxic to the cells in culture. We also observe a disintegration of the plasma membrane of amyloid-producing cells with SEM (Fig. S9). The vesicular lipid inclusions are also seen if amyloid deposits were formed by cells that were kept under serum-free conditions and

in the absence of HDL, demonstrating that the cells are a cause of the encountered lipid structures (Fig. S10).

We can discern, in the recorded tomograms, two modes by which fibrils interact with the lipids. These modes depend on whether fibrils contact the lipid bilayers through their tips (Fig. 3E–G) or through their lateral surfaces (Fig. 3H–J). Interactions with the fibril tip can lead to a significant distortion of the membrane structure at the contact point (Fig. 3E–G). These interactions are also more abundant and occur with 6% of the fibril tips in lipid-rich tomograms, whereas only 3% of the cumulative length of the same fibrils in the same tomogram is in lateral contact with the lipid membranes. In addition, we frequently saw fibrils form a cage around the lipid inclusion (Fig. 3K), apparently avoiding direct interactions and suggesting that lateral fibril–lipid interactions are more incidental in our system or restricted to certain membrane regions only. In our tomograms, we almost never saw fibrils that penetrated through a lipid bilayer.

Discussion

In this study, we have used electron tomography to investigate the deposit structure of the fibrils formed by a cell culture model of AA amyloidosis. Our analysis reveals three types of network structures that we term fibril meshwork, fibril bundle, and amyloid star. These data are consistent with previous analyses of histological tissue sections that used topographical reactions or conventional TEM methods that solely reported 2D projections of a tissue slice but did not generate 3D structural data. Such 2D data have been reported, for example, for $A\beta$ fibrils in Alzheimer's disease and for transthyretin-derived fibrils in ATTR amyloidosis, as well as for fibril deposits formed in other types of systemic amyloidosis, notably including AA. The observed features are consistent with star-like assemblies (27–29) and fibril bundles (8, 30–32), as well as with fibril meshwork structures (8). Based on the currently used tomographic techniques, 3D structural views of the respective network structures can now be provided.

The investigated fibrils are toxic when added to other cells (Fig. S4), and all the above examples of similarly structured amyloid deposits refer to pathogenic amyloids within the extracellular space. It is thus possible that intracellular or cytoplasmic cross- β filaments may have a different structural organization, specifically

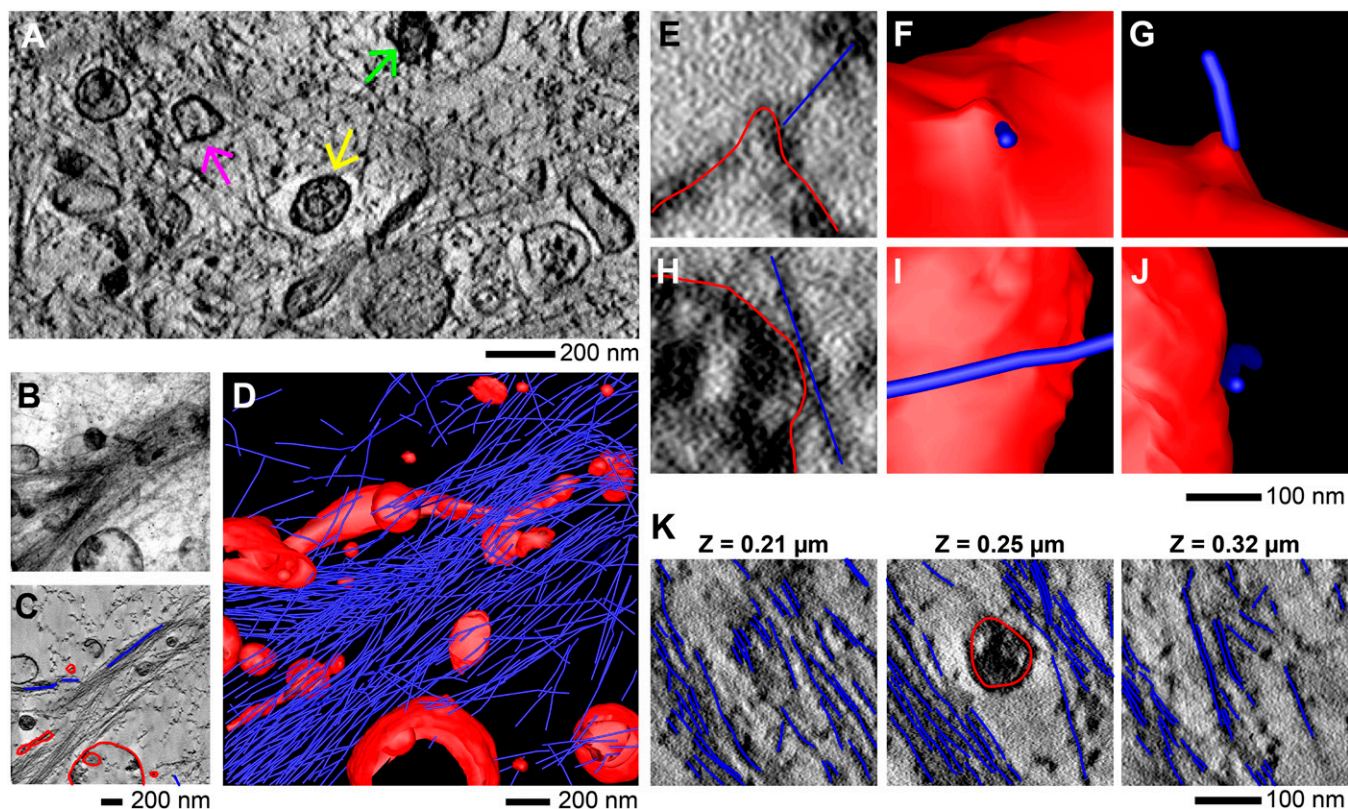


Fig. 3. Vesicular lipid inclusions and fibril–lipid interactions in amyloid deposits. (A) Virtual section through a tomogram of an amyloid deposit with extensive lipid inclusions. The green arrow points to a densely filled apoptotic body, the yellow arrow points to a multivesicular structure, and the magenta arrow points to a vesicle with low-electron-dense content. A 2D projection (B), virtual section (C), and 3D model (D) of an amyloid bundle show extensive lipid inclusions. (E–J) Tomogram of a deposit with lipid inclusions. Virtual sections (E and H) and regions of the 3D model (F, G, I, and J) are shown. (E–G) Lipid interaction via the fibril tip, distorting the lipid bilayer and producing a notable hump at the interaction site. (H–J) Lipid interaction via the lateral surface of the fibril. (K) Series of virtual sections showing a vesicular inclusion where the inclusion displaces a fibril bundle without making direct lateral contacts to the filaments. The figures in G and J are rotated by 90° relative to F and I.

if they are of functional relevance to their host cells. Examples are the fibrils formed from sup35 or pml17 protein. Sup35-derived fibrils play a role in phenotypic inheritance in yeast cells (33) and were found to adopt ring-like assemblies underneath the plasma membrane or dot-like cytoplasmic inclusions with a regular mosaic structure (33). Pml17 fibrils are important for melanosome formation, and tomographic studies revealed intracellular sheet like-assemblies that consist of parallel fibrils of pml17 protein (34). The different network structures of these intracellular filaments compared with the presently investigated extracellular amyloids raise the possibility that intracellular networks are influenced by one or several intracellular factors modifying their assembly.

Such modifying factors may also exist for the extracellular fibril networks because the fibrils structuring the presently analyzed deposits do not show a random orientation but structural order in terms of a fibril bundle or an amyloid star. The factors responsible for these effects could arise from the environment in which fibril formation takes place, for example, if fibrils form within a cavity or under shear flow conditions that induce a preferential orientation of the formed filaments (24, 35). Alternatively, it is possible that fibrils interact with molecules like GAGs or lipids that exhibit regular surfaces and were shown to affect the nucleation and growth of amyloid-like fibrils in vitro (36, 37). However, lipid vesicles may also form obstacles that sterically restrict the room in which fibril growth can take place, and several of the presently analyzed fibril bundles have apparently grown around a preexisting vesicle (Fig. 3K).

A second possible source of ordering factors is the fibrillation mechanism. For example, if fibrils become nucleated on the surface of a preexisting fibril (38), it is possible that the seed partially orients the daughter filament. Furthermore, total internal reflection fluorescence microscopy revealed the outgrowth of amyloid-like fibrils in vitro and the formation of fibril bundles due to fibril branching reactions (39) or the formation of star-like spherulites due to a radial extension of fibrils from a seed (40, 41).

A particularly interesting feature of the recorded tomograms is the association of the fibril deposits with lipids. Lipids have long been known to be present in pathological amyloid deposits (16, 24). Thin layer chromatography previously established their molecular composition and enrichment in cholesterol, cholesterol esters, and sphingolipids (16), whereas conventional TEM analyses reported the presence of spherical lipid inclusions in histological sections of amyloid-laden tissues (24), reminiscent of the vesicular structures seen here by tomography.

Lipid inclusions may interact with the fibrils, and respective interactions occur either via the fibril tip or through the lateral fibril surface. We find here that the interactions via the fibril tip are more abundant and strong enough to distort the lipid bilayer structure locally (Fig. 3E–G). They possibly involve hydrophobic interactions between the fatty acid tails and the relatively hydrophobic fibril core that is exposed at the fibril tip, as suggested by a recent structural model of A β (1–42) fibrils (42). Interactions of the tips of in vitro-formed β 2-microglobulin fibrils were previously observed with artificial liposomes and found to perturb the structural integrity of their lipid bilayer structures (43), one possible

toxic mechanism of amyloid fibrils (25, 43). Interactions of the lateral fibril surface with the lipid bilayer are likely to involve greater contributions from polar or electrostatic groups and may underlie the binding of cross- β fibrils to lipid-enveloped viral particles in the course of viral infection enhancements (26). The present study, as well as the previous β 2-microglobulin study, can detect such lateral interactions, but they are particularly rare in the present case.

Having established electron tomography as a tool to investigate the structure of disease-associated amyloid deposits, it is now possible to apply this method to other biological samples, such as histological sections, and to explore the 3D structure and pathogenic effects of in vivo-formed amyloid deposits on their neighboring tissues. Moreover, cross- β fibrils have recently given rise to biotechnological utilities, such as hydrogels, cell growth support structures, filtration units for purification, and enhancers of viral infections (26, 44–46). These applications may also depend on the fibril network structure, and through the presently described techniques, it is now possible to characterize the 3D structure of these assemblies as a prerequisite to fine-tuning their functions.

Materials and Methods

Growth of Amyloid Deposits in Cell Culture. J774A.1 cells (Sigma–Aldrich) were seeded in a 96-well plate (Greiner Bio-One) at a concentration of 350,000 cells per milliliter. The wells contained either sapphire disks (3 mm; M. Wohlwend GmbH) if samples were dedicated for SEM or TEM or glass coverslips if samples were produced for light microscopy (Thermo Fisher Scientific). Sapphire disks were pretreated by coating with a 20-nm-thick carbon layer using a Balzers BAF 300 (Bal-Tec) instrument. The coated disks were dried overnight in an oven (120 °C) and sterilized by UV irradiation at 320 nm for 10 min immediately before use. The cultured cells were always cultivated in an atmosphere containing 5% (vol/vol) CO₂ at 37 °C and in Dulbecco's modified Eagle's medium (Life Technologies) that was supplemented with 10% (vol/vol) of heat-inactivated FBS (Life Technologies) and 1% (vol/vol) of Antibiotic-Antimycotic (Life Technologies). To induce the formation of amyloid deposits, we added aliquots from stock solutions of SAA1 and HDL to the cell culture medium. We exchanged the cell culture medium, together with HDL and SAA1 if applicable, every 24 h or 48 h until the end of incubation.

The SAA1 stock was prepared by dissolving lyophilized murine SAA1.1 in distilled water at a concentration of 10 mg/mL. Residual trifluoroacetate was removed by washing the protein twice with pure water using a 3-kDa membrane filter (Amicon Ultra-0.5 mL 3K; Merck Millipore) that was centrifuged for 10 min at 16,900 $\times g$. The sample remaining in the membrane filter was filled up with pure water to adjust the protein concentration to 10 mg/mL. Elution of the protein from the membrane was done by inversion of the filter and centrifugation for 1 min at 100 $\times g$. Stock SAA1 solution was added to the culture to reach a final SAA1 concentration of 1 mg/mL. The stock solution of human HDL was obtained commercially (AppliChem). The amount of HDL stock that we added to the culture depended on the HDL concentration that was provided by the vendor based on the triglyceride content of the sample. Hence, the amount of HDL stock that we added was adjusted such that the final concentration of triglycerides in milligrams per milliliter was 9% (wt/vol) of the SAA1 protein concentration in milligrams per milliliter that we added to the culture supernatant.

Preparation of TEM Specimens Embedded in Epoxy Resin. Sapphire disks were removed from 96-well plates and plunged into 95% (vol/vol) 1-hexadecene (Sigma–Aldrich). Excess solution was removed via touching onto filter paper. Two sapphire disks were stacked up face-to-face, separated by a gold ring (diameter = 3.05 mm, central bore = 2 mm; Plano), mounted in a holder (Engineering Office, M. Wohlwend GmbH), and inserted into a Wohlwend HPF Compact 01 high-pressure freezer (Engineering Office, M. Wohlwend GmbH). The stack was disassembled with a set of pliers, and each sapphire disk was transferred into a separate precooled (–87 °C) 1.5-mL sample tube (Eppendorf). To each tube we added 1 mL of freeze substitution solution, which consisted of 0.2% (wt/vol) osmium tetroxide, 0.1% (wt/vol) uranyl acetate, and 5% (vol/vol) distilled water in acetone. The tubes were warmed up to 0 °C over a period of 24 h. Finally, they were left to equilibrate at room temperature for 1 h. The solution was removed, and the samples were washed with 1 mL of 100% (vol/vol) acetone. Each sample was incubated in an ascending epoxy resin (Fluka) series [33%, 50%, or 66% (vol/vol) epoxy resin in acetone]. Each incubation step (1 mL) lasted for 1 h at room temperature. The solution was replaced with 1 mL of pure epoxy resin and incubated for 24 h at room temperature. Afterwards, the sample was transferred into a new sample tube (Eppendorf) containing

0.25 mL of pure epoxy resin and heated to 60 °C for 24 h to polymerize the resin. The resin blocks were stored at room temperature.

TEM. The analysis of thin sections without acquisition of tilt angle series and of extracted fibrils on formvar-carbon-coated copper grids (Plano) and counterstained with 2% (wt/vol) uranyl acetate grids was done at 120 kV using a JEM-1400 electron microscope (Jeol) equipped with a VELETA 2,000 \times 2,000 side-mounted TEM camera (Olympus). Sections were mounted onto a 200 mesh, quadratic formvar-carbon-coated grid or on 300 mesh parallel copper grids (Plano) counterstained with 0.3% (wt/vol) lead citrate in water.

Scanning Transmission Electron Tomography. From the resin block, we cut 500-nm-thick sections with a microtome (Leica Ultracut UCT ultramicrotome) using a diamond knife (Diatome). The resin block was cut in the direction parallel to the plane of the sapphire disk, and the slice was placed onto a copper grid (300 mesh parallel) that was plasma-cleaned with an Edwards plasma cleaning system and dried for 10 min at room temperature. A droplet of 10% (wt/vol) poly-L-lysine (Sigma–Aldrich) in water was added onto the grid holding the slice and dried for 5 min on a heating block (37 °C). Afterward, we put 15 μ L of a solution of 15-nm colloidal gold particles (Aurion) that was diluted 1:1 with water onto each side of the grid. The gold particles serve as markers for image alignment in the processing of the electron tomograms. Finally, the grid holding the slice was coated on each side with a 5-nm carbon layer using a Balzers BAF 300 electron beam evaporation apparatus. The grid was plasma-cleaned with a Solarus Model 950 Advanced Plasma Cleaning System (Gatan) for 10 s immediately before electron microscopy. Image series at different tilt angles were recorded with a FEI-300 kV Titan scanning transmission electron microscope (FEI) operated at an acceleration voltage of 300 kV. Electron micrographs were recorded with a bright-field detector (FEI) at a size of 1,024 \times 1,024 pixels. A single-axis tilt-series was recorded from –72° to +72° using tilt increments of 1°. Hence, the final image series consisted of 145 original images. Each image was acquired using an exposure time of 18 s and a convergence angle of 0.58 mrad. From the acquired tilt angle series, we reconstructed the tomograms and produced a 3D model using the IMOD software package (version 4.7.6); that is, the individual images were first aligned to form an image stack. In the second step, the tomogram was computationally reconstructed using a weighted back-projection algorithm. The 3D model was generated by tracing the fibrils and lipid vesicles manually through the different virtual sections of the tomogram.

Measurement of the Fibril Width, Contour Length, and Persistence Length. The fibril width W , the contour length L , and the end-to-end distance R were determined from negative-stain TEM images of 500 cell culture-derived fibrils, 500 AA amyloid fibrils that were extracted from murine spleen, and 500 amyloid-like fibrils formed from murine SAA1 in vitro. Measurements were carried out using iTEM software (Olympus). The persistence length P was calculated from L and R using Eq. 1, assuming that the fibrils were deposited in a 2D manner on the grid surface in an energetically equilibrated conformation:

$$(R)^2 = 4PL * \left[1 - \frac{2P}{L} * \left(1 - e^{-\left(\frac{P}{L}\right)} \right) \right]. \quad [1]$$

The values of W in the tomograms were measured for 250 fibrils per deposit type by analysis of the virtual sections using GNU Image Manipulation Program 2 software (version 2.8.14). In addition, P has been calculated for all fibrils contained in the 3D models using Eq. 2. Because Eqs. 1 and 2 cannot be solved for P analytically, the solution has been approximated numerically using Newton's method (47), with a constant initial value of 1 and a target accuracy of 10^{–7}:

$$(R)^2 = 2PL * \left[1 - \frac{P}{L} * \left(1 - e^{-\left(\frac{P}{L}\right)} \right) \right]. \quad [2]$$

Induction of AA-Amyloid in Mice. AA amyloidosis was induced in a female 6-wk-old NMRI mouse as described (48). Animal experiments were conducted based on permission from the Thüringer Landesamt für Lebensmittelsicherheit und Verbraucherschutz Abteilung Gesundheitlicher Verbraucherschutz, Veterinärwesen, Pharmazie (registration no. 03-010/12). The animal was anesthetized with 480 mg/kg Ketamin (Inresa) and 64 mg/kg Rompun (Bayer) or 600 mg/kg isoflurane (Forene; Abbott) and killed by cervical dislocation, and the spleen was removed and stored at –80 °C or –20 °C.

ACKNOWLEDGMENTS. We thank Anastasia Weber and Beate Garbers for help in protein purification, C. Parthier and M. T. Stubbs (Martin-Luther-Universität Halle-Wittenberg) for access to their X-ray beam, and Dr. Maria

Strassburger (Hans Knoell Institute) for assistance in the animal experiments. This work was supported by the Grants FA 456/15-1 and HA 7138/2-1 from

the Deutsche Forschungsgemeinschaft (to M.F. and C.H.). G.T.W. is supported by the Swedish Research Council.

- Chiti F, Dobson CM (2006) Protein misfolding, functional amyloid, and human disease. *Annu Rev Biochem* 75:333–366.
- Sipe JD, et al. (2014) Nomenclature 2014: Amyloid fibril proteins and clinical classification of the amyloidosis. *Amyloid* 21(4):221–224.
- Hazenbergh BP (2013) Amyloidosis: A clinical overview. *Rheum Dis Clin North Am* 39(2):323–345.
- Eisenberg D, Jucker M (2012) The amyloid state of proteins in human diseases. *Cell* 148(6):1188–1203.
- Fändrich M, Schmidt M, Grigorieff N (2011) Recent progress in understanding Alzheimer's β -amyloid structures. *Trends Biochem Sci* 36(6):338–345.
- Pepys MB (2006) Amyloidosis. *Annu Rev Med* 57:223–241.
- Obici L, Merlini G (2012) AA amyloidosis: Basic knowledge, unmet needs and future treatments. *Swiss Med Wkly* 142:w13580.
- Bergström J, et al. (2005) Amyloid deposits in transthyretin-derived amyloidosis: Cleavage transthyretin is associated with distinct amyloid morphology. *J Pathol* 206(2):224–232.
- Thal DR, Walter J, Saido TC, Fändrich M (2015) Neuropathology and biochemistry of A β and its aggregates in Alzheimer's disease. *Acta Neuropathol* 129(2):167–182.
- Baumeister W (2004) Mapping molecular landscapes inside cells. *Biol Chem* 385(10):865–872.
- Shirahama T, et al. (1990) Amyloid enhancing factor-loaded macrophages in amyloid fibril formation. *Lab Invest* 62(1):61–68.
- Kluve-Beckerman B, Manaloor J, Liepnieks JJ (2001) Binding, trafficking and accumulation of serum amyloid A in peritoneal macrophages. *Scand J Immunol* 53(4):393–400.
- Elimova E, Kisilevsky R, Szarek WA, Ancsin JB (2004) Amyloidogenesis recapitulated in cell culture: A peptide inhibitor provides direct evidence for the role of heparan sulfate and suggests a new treatment strategy. *FASEB J* 18(14):1749–1751.
- Westermarck GT, Fändrich M, Westermarck P (2015) AA amyloidosis: Pathogenesis and targeted therapy. *Annu Rev Pathol* 10:321–344.
- Kluve-Beckerman B, Liepnieks JJ, Wang L, Benson MD (1999) A cell culture system for the study of amyloid pathogenesis. Amyloid formation by peritoneal macrophages cultured with recombinant serum amyloid A. *Am J Pathol* 155(1):123–133.
- Gellermann GP, et al. (2005) Raft lipids as common components of human extracellular amyloid fibrils. *Proc Natl Acad Sci USA* 102(18):6297–6302.
- Röcken C, Shakespeare A (2002) Pathology, diagnosis and pathogenesis of AA amyloidosis. *Virchows Arch* 440(2):111–122.
- Derebe MG, et al. (2014) Serum amyloid A is a retinol binding protein that transports retinol during bacterial infection. *eLife* 3:e03206.
- Lu J, Yu Y, Zhu I, Cheng Y, Sun PD (2014) Structural mechanism of serum amyloid A-mediated inflammatory amyloidosis. *Proc Natl Acad Sci USA* 111(14):5189–5194.
- Haupt C, et al. (2011) Pattern recognition with a fibril-specific antibody fragment reveals the surface variability of natural amyloid fibrils. *J Mol Biol* 408(3):529–540.
- Curtis H, Barnes SN (1989) *Biology* (Worth Publishers, New York), 5th Ed.
- Hine R (1999) *Membrane. The Facts on File Dictionary of Biology* (Checkmark, New York), 3rd Ed.
- Kuchel PW, Ralston GB (1988) *Theory and Problems of Biochemistry*, Schaum's Outlines (McGraw-Hill, New York).
- Sorenson GD, Bari WA (1968) Murine amyloid deposits and cellular relationships. *Amyloidosis*, eds Mandema E, Ruinen L, Scholten JH, Cohen AS (Excerpta Medica, Amsterdam), pp 58–73.
- Butterfield SM, Lashuel HA (2010) Amyloidogenic protein-membrane interactions: Mechanistic insight from model systems. *Angew Chem Int Ed Engl* 49(33):5628–5654.
- Meier C, Weil T, Kirchhoff F, Münch J (2014) Peptide nanofibrils as enhancers of retroviral gene transfer. *Wiley Interdiscip Rev Nanomed Nanobiotechnol* 6(5):438–451.
- Westermarck P (2015) Localized amyloidosis and amyloidoses associated with aging outside the central nervous system. *Amyloid and Related Disorders Current Clinical Pathology*, eds Picken MM, et al. (Springer, Cham, Switzerland), pp 95–120.
- Wisniewski HM, Wegiel J, Wang KC, Lach B (1992) Ultrastructural studies of the cells forming amyloid in the cortical vessel wall in Alzheimer's disease. *Acta Neuropathol* 84(2):117–127.
- Gondo T, et al. (1993) Localized amyloidosis in squamous cell carcinoma of uterine cervix: electron microscopic features of nodular and star-like amyloid deposits. *Virchows Arch A Pathol Anat Histopathol* 422(3):225–231.
- Romhányi G (1949) Ueber die submikroskopische Struktur des Amyloids. *Schweiz Z Pathol Bakteriol* 12(3):253–262. German.
- Shirahama T, Cohen AS (1973) An analysis of the close relationship of lysosomes to early deposits of amyloid. Ultrastructural evidence in experimental mouse amyloidosis. *Am J Pathol* 73(1):97–114.
- Stalder M, Deller T, Staufenberg M, Jucker M (2001) 3D-Reconstruction of microglia and amyloid in APP23 transgenic mice: No evidence of intracellular amyloid. *Neurobiol Aging* 22(3):427–434.
- Saibil HR, et al. (2012) Heritable yeast prions have a highly organized three-dimensional architecture with interfiber structures. *Proc Natl Acad Sci USA* 109(37):14906–14911.
- Hurbain I, et al. (2008) Electron tomography of early melanosomes: Implications for melanogenesis and the generation of fibrillar amyloid sheets. *Proc Natl Acad Sci USA* 105(50):19726–19731.
- Mangione PP, et al. (2013) Structure, folding dynamics, and amyloidogenesis of D76N β 2-microglobulin: Roles of shear flow, hydrophobic surfaces, and α -crystallin. *J Biol Chem* 288(43):30917–30930.
- Cohlberg JA, Li J, Uversky VN, Fink AL (2002) Heparin and other glycosaminoglycans stimulate the formation of amyloid fibrils from α -synuclein in vitro. *Biochemistry* 41(5):1502–1511.
- Galvagnion C, et al. (2015) Lipid vesicles trigger α -synuclein aggregation by stimulating primary nucleation. *Nat Chem Biol* 11(3):229–234.
- Cohen SI, Vendruscolo M, Dobson CM, Knowles TP (2012) From macroscopic measurements to microscopic mechanisms of protein aggregation. *J Mol Biol* 421(2–3):160–171.
- Andersen CB, et al. (2009) Branching in amyloid fibril growth. *Biophys J* 96(4):1529–1536.
- Ban T, et al. (2006) Real-time and single fibril observation of the formation of amyloid beta spherulitic structures. *J Biol Chem* 281(44):33677–33683.
- Krebs MR, Domike KR, Donald AM (2009) Protein aggregation: More than just fibrils. *Biochem Soc Trans* 37(Pt 4):682–686.
- Schmidt M, et al. (2015) Peptide dimer structure in an A β (1–42) fibril visualized with cryo-EM. *Proc Natl Acad Sci USA* 112(38):11858–11863.
- Milanesi L, et al. (2012) Direct three-dimensional visualization of membrane disruption by amyloid fibrils. *Proc Natl Acad Sci USA* 109(50):20455–20460.
- Vauthey S, Santoso S, Gong H, Watson N, Zhang S (2002) Molecular self-assembly of surfactant-like peptides to form nanotubes and nanovesicles. *Proc Natl Acad Sci USA* 99(8):5355–5360.
- Cherny I, Gazit E (2008) Amyloids: Not only pathological agents but also ordered nanomaterials. *Angew Chem Int Ed Engl* 47(22):4062–4069.
- Bolisetty S, Mezzenga R (2016) Amyloid-carbon hybrid membranes for universal water purification. *Nat Nanotechnol* 11(4):365–371.
- Kelley CT (1995) *Iterative Methods for Linear and Nonlinear Equations* (SIAM, Philadelphia).
- Lundmark K, Vahdat Shariatpanahi A, Westermarck GT (2013) Depletion of spleen macrophages delays AA amyloid development: A study performed in the rapid mouse model of AA amyloidosis. *PLoS One* 8(11):e79104.
- Ganowiak K, Hultman P, Engström U, Gustavsson A, Westermarck P (1994) Fibrils from synthetic amyloid-related peptides enhance development of experimental AA-amyloidosis in mice. *Biochem Biophys Res Commun* 199(1):306–312.
- Silverman BW (1986) *Density Estimation for Statistics and Data Analysis* (CRC, London).
- Scott DW (2015) *Multivariate Density Estimation: Theory, Practice and Visualization* (Wiley, New York), 2nd Ed.
- Snyder JP (1987) *Map Projections—A Working Manual* (U.S. Government Publishing Office, Washington, DC).